

# The role of hadronic cascades in GRB models of efficient neutrino production

Maria Petropoulou<sup>1,2</sup> \*

<sup>1</sup>*Department of Physics and Astronomy, Purdue University, 525 Northwestern Avenue, West Lafayette, IN, 47907, USA*

<sup>2</sup> *NASA Einstein Postdoctoral Fellow*

Received.../Accepted...

## ABSTRACT

We investigate the effects of hadronic cascades on the gamma-ray burst (GRB) prompt emission spectra in scenarios of efficient neutrino production. By assuming a fiducial GRB spectrum and a power-law proton distribution extending to ultra-high energies, we calculate the proton cooling rate and the neutrino emission produced through photopion processes. For this, we employ a numerical code that follows the formation of the hadronic cascade by taking into account non-linear feedback effects, such as the evolution of the target photon field itself due to the contribution of secondary particles. We show that in cases of efficient proton cooling and subsequently efficient high-energy neutrino production, the emission from the hadronic cascade distorts and may even dominate the GRB spectrum. Taking this into account, we constrain the allowable values of the ratio  $\eta_p = L_p/L_\gamma$ , where  $L_p$  and  $L_\gamma$  are the isotropic equivalent proton and prompt gamma-ray luminosities. For the highest value of  $\eta_p$  that does not lead to the dominance of the cascading emission, we then calculate the maximum neutrino luminosity from a single burst and show that it ranges between  $(0.01 - 0.6)L_p$  and  $(0.5 - 1.4)L_\gamma$  for various parameter sets. We discuss possible implications of other parameters, such as the magnetic field strength and the shape of the initial gamma-ray spectrum, on our results. Finally, we compare the upper limit on  $\eta_p$  derived here with various studies in the field, and we point out the necessity of a self-consistent treatment of the hadronic emission in order to avoid erroneously high neutrino fluxes from GRB models.

**Key words:** neutrinos – radiation mechanisms: non-thermal – gamma ray burst: general

## 1 INTRODUCTION

Gamma-ray bursts (GRBs) are candidate sites of proton acceleration to ultra-high energies (UHE) (Waxman 1995; Vietri 1995) and, therefore, potential sources of high-energy (HE) neutrino emission (Paczynski & Xu 1994; Waxman & Bahcall 1997). The problem of GRB neutrino production has been considered by many authors (Murase 2008; Mannheim et al. 2001; Dermer & Atoyan 2003; Guetta et al. 2004; Asano 2005; Rachen & Mészáros 1998; Baerwald et al. 2013; Reynoso 2014) and it may gain even more interest under the light of the recent IceCube HE neutrino detection (IceCube Collaboration 2013; Aartsen et al. 2014).

Another aspect of GRB models for neutrino production is the formation of hadronic cascades (HC), i.e. cascades consisting of relativistic electron-positron pairs, initiated

by photopion interactions of UHE protons with the GRB prompt radiation which, in this framework, serves as the target field. The emission produced by such cascades has some interesting implications as far as the prompt emission is concerned. For example, it has been proposed as an alternative explanation for the underlying power-law components seen in some bright bursts (e.g. GRB 090902B (Abdo et al. 2009); GRB 080319B (Racusin et al. 2008)), which extend from the hard X-rays up to GeV energies and do not agree with simple extrapolations of the MeV spectrum (Asano et al. 2010). More general studies regarding the emission signatures of hadronic cascades in the GeV and TeV energy bands and how these can be used as diagnostic tools of UHECR acceleration in GRBs have been made by various authors (e.g. Böttcher & Dermer 1998; Asano & Inoue 2007; Asano et al. 2009). One common feature of the aforementioned studies is that the emission produced by the hadronic cascade does not dominate over the MeV emission of the burst, which further implies that the proton cooling and neutrino pro-

\* E-mail: mpetropo@purdue.edu

duction through photopion interactions are not very efficient. On the other hand, models that focus on the GRB neutrino emission require high efficiency while at the same time they neglect any effects of the hadronic cascade on the MeV part of the GRB spectrum (e.g. Abbasi et al. 2010; Zhang & Kumar 2013).

In the present work we try to bridge the gap between the two approaches by demonstrating, in the most general way possible, the gradual dominance of the cascading emission over the MeV (and/or GeV) part of the spectrum as the efficiency in neutrino production progressively increases. For this, we simulate the GRB prompt emission spectrum as a grey-body photon field, which can be characterized only by two parameters, i.e. its effective temperature  $T$  and its compactness  $\ell_\gamma$ . Using this as a fixed target field, we gradually increase the injection luminosity of protons, or equivalently, their compactness, up to that value where the emission from the HC begins to affect the gamma-ray spectrum. The dominance of the HC sets, therefore, an upper limit on  $L_p$  and on the ratio  $\eta_p = L_p/L_\gamma$ , where  $L_p$  and  $L_\gamma$  are the proton and prompt gamma-ray (isotropic) luminosities, respectively, as measured in the observer's frame. For the maximum value of this ratio ( $\eta_{p,\max}$ ) we then calculate the neutrino production efficiency ( $\xi_\nu$ ) as well as the efficiency in the injection of secondary pairs and photons ( $\xi_{\text{sec}}$ ) into the HC. We show that the upper limit of  $\eta_p$  is anticorrelated with the  $\ell_\gamma$ ,  $\xi_\nu$  and  $\xi_{\text{sec}}$ . As a next step, we investigate the robustness of our findings by repeating the procedure for a higher magnetic field strength and a gamma-ray spectrum that can be described by the more accurate for GRBs Band function (Band et al. 2009). We comment also on the role of the Bethe-Heitler process in the formation of the HC. Finally, we calculate  $\ell_\gamma$  for different parameter sets used in the literature and compare the values of 'proton loading' used therein, i.e. the ratio of proton to gamma-ray luminosities (or energy densities), with our upper limit  $\eta_{p,\max}$ .

The present work is structured as follows: in §2 we describe our methods and we then present the numerical code used for our simulations in §3. We continue in §4 with the presentation of our results and discuss the effects of other parameters, such as the spectral shape of the initial gamma-ray emission. In §5 we compare our upper limit imposed on the 'proton loading' with that used in various cases in the literature. We conclude in §6 with a summary and a discussion of our results.

## 2 METHODS

In the present study we do not attempt a self-consistent calculation of the GRB prompt emission nor we pinpoint the GRB emission itself. Instead, we focus on the formation of the hadronic cascade and the self-consistent calculation of the neutrino emission after taking into account the modification of the initial gamma-ray spectrum. We choose, first, to depict the prompt emission spectrum as a grey-body photon field instead of using the typical Band function for two reasons: the effects of the cascade emission on the primary photon field become more evident and only two parameters, namely the photon compactness  $\ell_\gamma$  and the effective temperature  $T$ , are required for its description. The effects of

a Band-shape photon spectrum on our results will be discussed separately in §4.4.2.

We assume that at a distance  $r$  from the central engine protons are accelerated into a power-law distribution with index  $p$  to ultra-high energies (UHE), e.g.  $E_p < 10^{18}$  eV in the comoving frame, and are subsequently injected at a constant rate into a spherical region<sup>1</sup> of size  $r_b$  that moves outwards from the central engine with Lorentz factor  $\Gamma$ . This region is equivalent to the shell of shocked ejecta in the internal shock scenario, and has a comoving width  $r_b \simeq r/\Gamma$  (for reviews, see Piran 2004; Zhang & Mészáros 2004).

We further assume that the region contains a magnetic field of strength  $B$  (in the comoving frame), which is usually related to the jet kinetic luminosity  $L_j$  through the parameter  $\epsilon_B$  as follows:

$$\epsilon_B L_j = c B^2 \Gamma^2 r^2. \quad (1)$$

Protons with gyroradii larger than the size  $r_b$  cannot be confined, and thus escape from the region (Hillas 1984). This sets a maximum Lorentz factor that is given by

$$\gamma_H = \frac{e B r_b}{m_p c^2}. \quad (2)$$

In principle, the maximum proton energy is given by the minimum of  $\gamma_H$  and  $\gamma_{\text{sat}}$ , where the latter denotes the saturation energy of the acceleration process due to energy losses. For the parameters used throughout the text, we find that  $\gamma_H \lesssim \gamma_{\text{sat}}$  (see Appendix B). For this, we set  $\gamma_{\text{max}} = \gamma_H$ . The total proton injection luminosity  $L_p$ , which is just a fraction of  $L_j$ , can be used for defining the proton injection compactness as:

$$\ell_p^{\text{inj}} = \frac{\sigma_T L_p}{4\pi r_b \Gamma^4 m_p c^3}. \quad (3)$$

Although electron acceleration at high energies is also expected to take place, here, in our attempt to minimize the number of free parameters, we assume that the injection luminosity of primary relativistic electrons is much lower than that of protons, making their contribution to the overall photon emission negligible.

The following parameters were kept fixed in all our numerical simulations, unless stated otherwise:  $\Gamma = 225$ ,  $r_b = 10^{12}$  cm,  $B = 960$  G,  $\gamma_{\text{max}} = 10^{8.6}$  and  $T = 10^7$  K. From this point on, we will refer to this parameter set as the benchmark case. For these values, the typical pulse duration in the internal shock scenario would be  $\delta t \approx r_b/c\Gamma = 0.15$  s, while  $\epsilon_B \simeq 2 \times 10^{-3}$  for  $L_j = 3 \times 10^{52}$  erg/s.<sup>2</sup> For a given pair of  $r_b$  and  $\Gamma$ , different values of  $\ell_\gamma$  correspond to different  $\gamma$ -ray (isotropic) luminosities ( $L_\gamma$ ), since the photon compactness is defined as

$$\ell_\gamma = \frac{\sigma_T L_\gamma}{4\pi r_b \Gamma^4 m_e c^3} \quad (4)$$

In particular, we chose the following set of  $\ell_\gamma$  values, namely  $\{0.07, 0.22, 0.7, 2.2, 7.0\}$ , which corresponds to prompt gamma-ray luminosities in the range  $L_\gamma = 10^{50} - 10^{52}$  erg/s with a logarithmic step of 0.5. Then, for each

<sup>1</sup> The assumption of a spherical region is valid as long as the beaming angle  $1/\Gamma$  is smaller than the opening angle of the jet, which holds during the GRB prompt phase.

<sup>2</sup> The choice of a low  $\epsilon_B$  value will be justified later on.

value of  $\ell_\gamma$ , we performed a series of numerical simulations where we increased  $\ell_p^{\text{inj}}$  over its previous value by a fixed logarithmic step  $\delta x$ .

The method outlined above highlights the main difference between our approach and the one usually adopted in the literature (e.g. Asano & Inoue 2007; Asano et al. 2009). Here, we use as free parameters the gamma-ray and proton injection compactnesses instead of  $\Gamma$ ,  $r$ ,  $\delta t$ ,  $L_\gamma$  and  $L_p$ , since only the former are the intrinsic quantities of the physical system. Note that very different combinations of  $\Gamma$ ,  $r$ ,  $\delta t$ ,  $L_\gamma$  may lead to the same  $\ell_\gamma$  and to similar derived properties of the lepto-hadronic system, such as the neutrino production efficiency.

### 3 NUMERICAL CODE

In order to study the formation of the hadronic cascade and its effects on the multiwavelength photon spectrum, we employ the time-dependent numerical code as presented in Dimitrakoudis et al. (2012) – hereafter DMPR12. This follows the evolution of protons, neutrons, secondary pairs, photons and neutrinos by solving the coupled integro-differential equations that describe the various distributions. The coupling of energy losses and injection introduces a self-consistency in this approach that allows the study of the system at various conditions, e.g. in the presence of non-linear electromagnetic (EM) cascades (see also Petropoulou & Mastichiadis 2012 for a relevant discussion). Although details can be found in DMPR12, for the sake of completeness, we summarize in Table 1 the physical processes that are included in the code.

Photohadronic interactions are modelled using the results of Monte Carlo simulations. In particular, for Bethe-Heitler pair production the Monte Carlo results by Protheroe & Johnson (1996) were used (see also Mastichiadis et al. 2005). Photopion interactions were incorporated in the time-dependent code by using the results of the Monte Carlo event generator SOPHIA (Mücke et al. 2000), which takes into account channels of multipion production for interactions much above the threshold.

Synchrotron radiation of muons was not included in the version of the code presented in DMPR12 and for the exact treatment we refer the reader to Dimitrakoudis et al. (2014). As synchrotron cooling of pions is not yet included in the numerical code, we restricted our analysis to cases where the effects of pion cooling are minimal.

Pairs that cool down to Lorentz factors  $\gamma \sim 1$  contribute to the Thomson depth and they are treated as a separate population with  $kT_e \ll m_e c^2$  (Lightman & Zdziarski 1987). For the pair annihilation and photon downscattering processes we followed Coppi & Blandford (1990) and Lightman & Zdziarski (1987), respectively (for more details see Mastichiadis & Kirk 1995). For completeness, we note that the limits on  $\eta_p$  derived in §4 would have been even more strict if photon downscattering was not taken into account, or cooling of pairs down to non-relativistic temperatures was not possible.

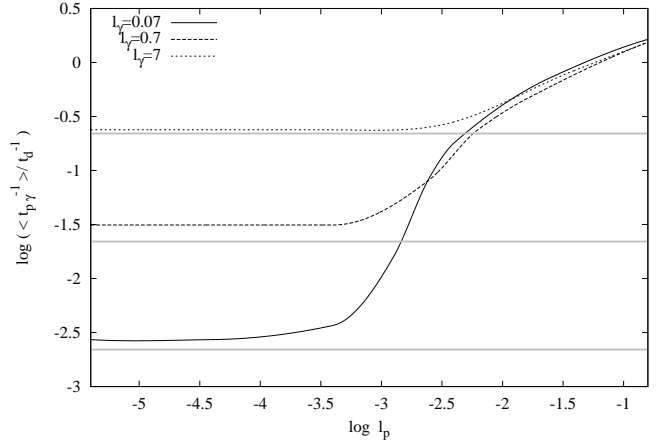


**Figure 1.** Photopion cooling rate (in units of  $c/r_b$ ) of protons with  $\gamma_p = 10^6 > E_{\text{th}}/1.4kT \simeq 10^5$ , where  $E_{\text{th}} \simeq 0.15$  GeV, as a function of the proton injection compactness  $\ell_p^{\text{inj}}$  for three values of the gamma-ray compactness marked on the plot. For comparison reasons, the cooling rate given by eq. (5) is plotted with grey lines.

## 4 RESULTS

### 4.1 Proton energy loss rate

First, we show that for high enough proton injection compactnesses, photons produced through the hadronic cascade contribute to the target photon field for photopion interactions and therefore enhance the respective proton energy loss rate. For this, we compare the analytic expression for the energy loss rate on a grey-body photon field of certain  $\ell_\gamma$  and  $T$  with the one derived numerically after taking into account the modification of the photon spectrum because of the cascade. It can be shown (for more details, see Appendix A) that the fractional energy loss rate of protons with Lorentz factor  $\gamma_p > \gamma_{\text{th}} = E_{\text{th}}/1.4kT$ , where  $E_{\text{th}} \simeq 0.15$  GeV, is

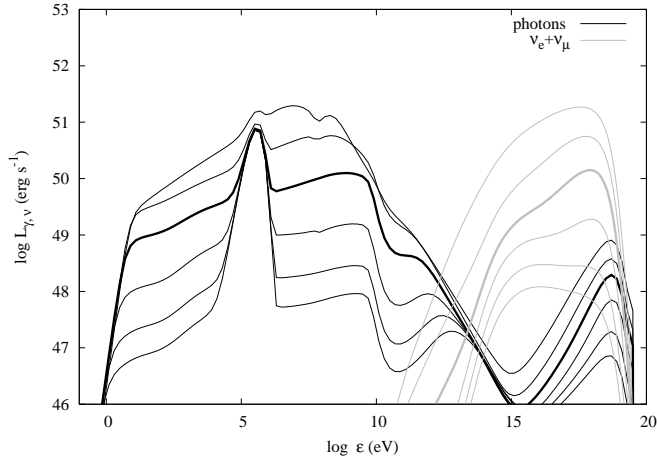
$$t_{p\gamma}^{-1} \simeq 5 \times 10^{-5} \frac{\ell_\gamma}{\Theta} t_d^{-1}, \quad (5)$$

where  $\Theta = kT/m_e c^2$  and  $t_d = r_b/c$ . As expected (see e.g. WB97, Aharonian 2000), the above expression does not depend on the proton injection compactness. The characteristic loss rate<sup>3</sup>, as derived by the simulations, where the feedback on the target field is taken into account in a self-consistent way, is plotted against  $\ell_p^{\text{inj}}$  in Fig. 1 for three values of  $\ell_\gamma$  marked on the plot. In all cases, the energy loss rate is constant and in agreement with the analytic expression (5), shown with grey lines in Fig. 1, only up to a certain value of  $\ell_p^{\text{inj}}$ . Its subsequent rapid increase is a sign of the modification of the initial photon spectrum because of the hadronic cascade. Hence, the analytic estimates of the fraction of energy lost by proton to pions can be considered only as a lower limit.

<sup>3</sup> The loss rate is calculated by  $\langle t_{p\gamma}^{-1} \rangle = \int d\gamma_p \gamma_p n_p(\gamma_p) \dot{P}_{p\gamma} / \int d\gamma_p \gamma_p n_p(\gamma_p)$ , where  $n_p$  is the steady-state proton distribution.

**Table 1.** Physical processes that act as injection (source) and loss terms in the kinetic equations of each species.

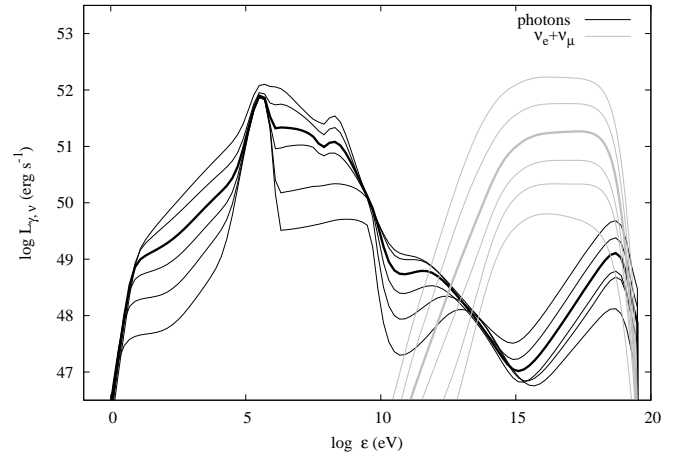
protons	neutrons	pions	muons	relativistic pairs	photons	neutrinos
Injection						
external $p\gamma^a$ $\beta$ -decay	$p\gamma$	$p\gamma$	$p\gamma$	$p\gamma$ BH <sup>b</sup> pair production $\gamma\gamma$ pair production	neutral pion decay proton synchrotron electron synchrotron muon synchrotron inverse Compton	$p\gamma$ $\beta$ -decay
Loss						
$p\gamma$ BH synchrotron escape	$p\gamma$ $\beta$ -decay escape	decay	decay synchrotron	synchrotron inverse Compton annihilation escape	$\gamma\gamma$ pair production synchrotron self-absorption Compton downscattering escape	escape

<sup>a</sup> photopion process<sup>b</sup> Bethe-Heitler process**Figure 2.** Observed photon and neutrino spectra obtained for  $\ell_\gamma = 0.7$  and values of the proton injection compactness starting from  $\ell_p = 10^{-3.4}$  (bottom curve) up to  $\ell_p = 10^{-1.4}$  (upper curve) with logarithmic increments of 0.4. The last spectra before the dominance of the hadronic cascade are shown with thick lines.

## 4.2 Photon and neutrino emission

The modification of the photon spectrum due to the emission from the secondaries produced in the hadronic cascade is demonstrated in Figs. 2 and 3, where we plot the multiwavelength photon spectra (black lines) in the observer's frame for two indicative values of the gamma-ray compactness, namely  $\ell_\gamma = 0.7$  and 7. For our choice of  $\Gamma$  and  $r_b$  (see §2) these correspond to observed gamma-ray luminosities  $L_\gamma = 10^{51}$  and  $10^{52}$  erg/s, respectively. The neutrino ( $\nu_e + \nu_\mu$ ) spectra (grey lines) are also plotted, for comparison reasons. In both figures, each spectrum is obtained by increasing  $\ell_p^{\text{inj}}$  (or equivalently  $L_p$ ) over its previous value with a logarithmic step  $\delta x$  – for the exact values see labels of the respective figures.

Above a certain value of  $\ell_p^{\text{inj}}$ , which depends on the value of  $\ell_\gamma$ , the emission from the hadronic cascade begins to either ‘cover’ the prompt emission spectrum (see top spectra in Figs. 2 and 3) or peak in the sub-GeV energy band with

**Figure 3.** Observed photon and neutrino spectra obtained for  $\ell_\gamma = 7$  and values of the proton injection compactness starting from  $\ell_p = 10^{-2.6}$  (bottom curve) up to  $\ell_p = 10^{-0.6}$  (upper curve) with logarithmic increments of 0.4. Thick lines have the same meaning as in Fig. 1.

a luminosity approximately equal to that of the MeV emission (see second spectrum from the top in Fig. 2). The latter is ruled out by the current status in observations (e.g. Dermer 2010). For illustration reasons, the spectra obtained just before the dominance of the HC are shown with thick lines in Figs. 2 and 3. From this point on, we will characterize cases that modify the initial MeV emission or have  $L_{(0.1-1)\text{GeV}} \gtrsim 0.2 - 0.3 L_{(0.1-1)\text{MeV}}$  commonly as ‘HC dominant’ cases. We note that if a stricter upper limit on the GeV luminosity was used this would also be reflected at the upper limit imposed on the proton to gamma-ray luminosity ratio discussed in the following section.

For a fixed  $\ell_\gamma$ , higher secondary emission and neutrino luminosities can be obtained by increasing the proton injection compactness. This is demonstrated in Fig. 4, where we plot the observed luminosities of protons, muon and electron neutrinos, photons and (0.1-1) MeV gamma-ray photons, for the case shown in Fig. 2. For low enough values of  $L_p$  the bolometric photon luminosity is actual equal to the lumi-

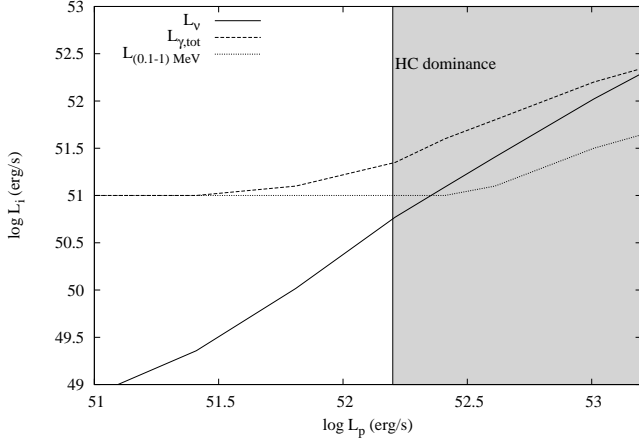


**Figure 4.** Log-log plot of the total neutrino luminosity (solid line), the bolometric photon luminosity (dashed line) and the (0.1–1) MeV gamma-ray luminosity (dotted line) as a function of the proton injection luminosity  $L_p$  for  $\ell_\gamma = 0.7$ . The grey colored area is obtained for  $L_p$  values that lead to the dominance of the HC emission.

nosity emitted in 0.1–1 MeV energy band. However, for  $L_p$  above a certain value, which for the particular example is  $\simeq 1.5 \times 10^{52}$  erg/s, we obtain  $L_\gamma^{\text{tot}} > L_{(0.1-1)\text{MeV}}$ . This indicates that the photon component of the hadronic cascade is no longer negligible. Moreover, we find that  $L_\nu \propto L_p^q$ , where  $q = 1$  for low enough  $L_p$  but  $q = 1.6$  for higher proton luminosities. This steeper than linear scaling relation between  $L_\nu$  and  $L_p$  is one more indication of the spectral modification due to the HC. Interestingly enough, the ratio of the neutrino to the bolometric photon luminosity becomes maximum only for proton luminosities leading to HC dominant cases (grey colored area in Fig. 4). Still, for the last case before the dominance of the HC, we find that the photon and neutrino components are energetically equivalent with  $L_\nu \simeq 0.3L_\gamma^{\text{tot}}$  (see also Table 2).

### 4.3 Maximum proton to gamma-ray luminosity ratio

For each value of  $\ell_\gamma$  we can derive a maximum value of the proton compactness above which the hadronic cascade significantly alters the GRB photon spectrum, as previously described. This can also be translated to a maximum value of the ratio  $\eta_p = L_p/L_\gamma$ , which in terms of compactnesses is written as  $\eta_p = \ell_p^{\text{inj}}(m_p/m_e)/\ell_\gamma^4$ . For these maximum values, we then derive (i) the ratio  $\eta_\nu = L_\nu/L_\gamma$ , (ii) the ratio  $\zeta_\nu = L_\nu/L_\gamma^{\text{tot}}$ , (iii) the production efficiency in neutrinos ( $\xi_\nu$ ), and (iv) the production efficiency in secondaries that contribute to the HC ( $\xi_{\text{sec}}$ ), where the efficiencies are defined as  $\xi_{\nu,\text{sec}} = L_{\nu,\text{sec}}/L_p = \ell_{\nu,\text{sec}}(m_e/m_p)/\ell_p^{\text{inj}}$ . Our results are summarized in Table 2 and a few things worth mentioning follow:

<sup>4</sup> An alternative definition for  $\eta_p$  would be  $\eta_p = L_p/L_\gamma^{\text{tot}}$ , where the superscript ‘tot’ denotes the bolometric photon luminosity. In the present work, however, we adopt the definition with the gamma-ray luminosity, as this appears mostly in the literature.

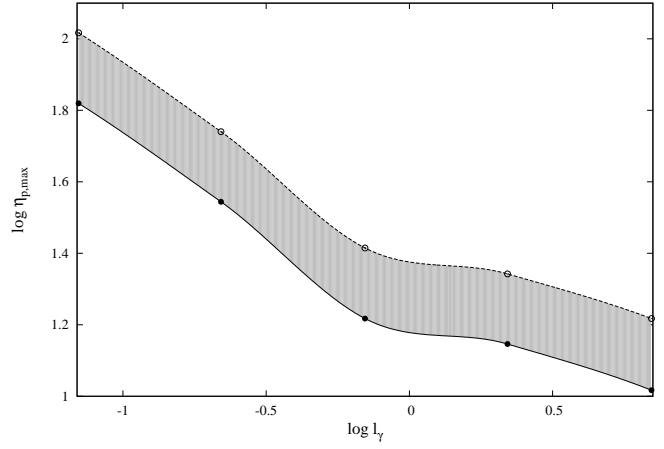


**Figure 5.** Log-log plot of  $\eta_{p,\text{max}}$  as a function of  $\ell_\gamma$ . The actual results of our simulations are shown with points while the lines are the result of interpolation. Results shown with filled circles/solid line are obtained for  $\eta_{p,\text{max}}$  while open circles/dashed line correspond to  $\eta_p = \eta_{p,\text{max}} 10^{\delta x}$ . The grey colored area denotes the uncertainty of the derived  $\eta_{p,\text{max}}$ .

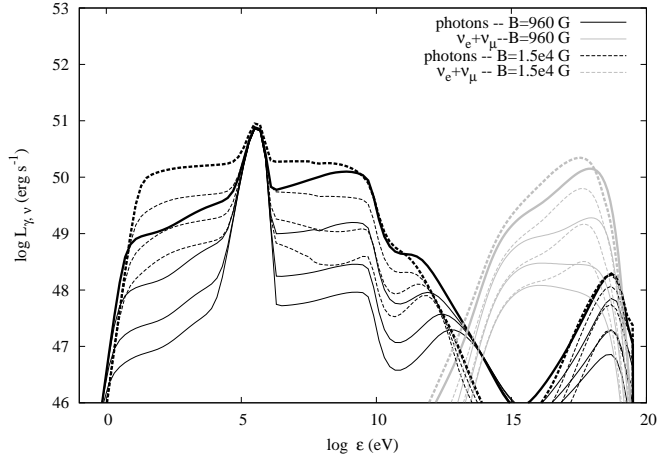
- the maximum value of  $\eta_p$  decreases as the photon compactness becomes larger. This is exemplified in Fig. 5. An extrapolation of our results to even larger values of  $\ell_\gamma$  (see e.g. Murase 2008; Zhang & Kumar 2013) would imply that  $L_p \approx (1 - 10)L_\gamma$  – see also §5 for a comparison with other works.
- there is an anticorrelation between the maximum allowable value of  $\eta_p$  and  $\xi_\nu$  ( $\zeta_\nu$ ) that reflects the fact that the upper limit imposed on  $\ell_p^{\text{inj}}$  by the HC, becomes more stringent as  $\ell_\gamma$  increases.
- the maximum ratio  $\zeta_\nu$  increases as the gamma-ray compactness becomes larger and may as high as 60% for  $\ell_\gamma \gtrsim 7$ .
- we find that  $\eta_{p,\text{max}} \propto 1/\xi_{\text{sec,max}}$ , which can be understood as follows the photon compactness from the cascade is defined as  $\ell_{\text{sec}} = \xi_{\text{sec}} \ell_p^{\text{inj}}(m_p/m_e)$  while  $\ell_p^{\text{inj}} = \eta_p \ell_\gamma (m_e/m_p)$ . Roughly speaking, the secondary photon emission will start affecting the overall photon spectrum, if  $\ell_{\text{sec}} \approx \alpha \ell_\gamma$  where  $\alpha$  is a numerical factor that contains all the details about the hadronic cascade and depends on a series of parameters, such as the magnetic field strength and the spectral shape of the secondary emission itself. Our results show, however, that  $\alpha$  varies less than a factor of 2 among the five parameter sets presented in Table 2, and we can, therefore, consider it a constant. By combining the above we find that  $\eta_{p,\text{max}} \approx \alpha/\xi_{\text{sec,max}} \propto 1/\xi_{\text{sec,max}}$ .

### 4.4 Effects of other parameters

In the previous section we demonstrated the effects of the HC on the photon and neutrino spectra but more importantly we showed that the HC imposes an upper limit on the ratio  $L_p/L_\gamma$ . Here, in an attempt to test the robustness of these results, we discuss in detail the effects of the magnetic field strength, of the initial spectral shape in gamma-rays, and of a larger value of  $\Gamma$ .

**Table 2.** Maximum values of various ratios-efficiencies derived for five values of the gamma-ray compactness.

$\ell_\gamma$	$\ell_\gamma^{\text{tot}}$	$\log \ell_{\text{p,max}}^{\text{inj}}$	$\eta_{\text{p,max}}$	$\eta_{\nu,\text{max}}$	$\zeta_{\nu,\text{max}}$	$\xi_{\text{sec,max}}$ (%)	$\xi_{\nu,\text{max}}$ (%)
0.07	0.2	-2.6	66	0.9	0.3	2.8	1.4
0.22	0.9	-2.4	35	1.4	0.35	7	4
0.7	1.5	-2.2	16.5	0.6	0.28	6.7	3.6
2.2	6.1	-1.8	14	1.4	0.5	15	10
7.0	15.7	-1.4	10.4	1.4	0.6	17.5	13

**Figure 6.** Comparison of photon and neutrino spectra for  $\ell_\gamma = 0.7$  and two values of the magnetic field strength, i.e.  $B = 960$  G and  $B = 1.5 \times 10^4$  G, shown with solid and dashed lines, respectively. The proton injection compactness ranges from  $10^{-3.4}$  (bottom) to  $10^{-2.2}$  (top). Thick lines have the same meaning as in Fig. 1.

#### 4.4.1 Magnetic field strength

In general, stronger magnetic fields enhance the cascade emission in two ways:

- through synchrotron radiation of secondary pairs, which leaves an imprint mainly at energies below 1 MeV in the comoving frame because of the strong photon attenuation that affects higher energy photons.
- through synchrotron cooling of muons and pions, which starts playing a role for high enough magnetic fields. This introduces more photons into the system, since part of the energy that would have been transferred to the neutrino component goes now into the photon component.

The effects of the magnetic field on the photon and neutrino emission are exemplified in Fig. 6. For the same proton injection compactness, we find that the flux of the HC emission increases, while the neutrino spectra become harder. The change of the neutrino spectral shape is non-trivial (see also Asano & Meszaros 2014) and it requires a self-consistent treatment, as it strongly depends on the shape of the target photon field. Finally, we find that the value of  $\eta_{\text{p,max}}$  is not significantly affected by the choice of the magnetic field, while the values of  $\xi_{\text{sec}}$  and  $\xi_\nu$  increase at most by a factor of two – see Table 3. Although synchrotron cooling of pions is not relevant for the benchmark case, it starts playing a role for the higher magnetic field strength considered here. In particular, we find that  $E_{\pi,c} \simeq E_{\pi,\text{max}}/10$ ,

where  $E_{\pi,\text{max}} \simeq 0.2\gamma_{\text{max}}m_{\text{p}}c^2 = 8 \times 10^{16}$  eV and  $E_{\pi,c}$  is the typical energy of a pion that cools due to synchrotron radiation before it decays. Since the numerical code does not account for the synchrotron losses of pions (see also §3), the results presented in this section should be considered as an upper limit. Inclusion of pion cooling would have a twofold effect on our results: first, the peak of the neutrino spectra would move towards smaller energies by approximately an order of magnitude and second, the resulting deficit in the neutrino luminosity would be balanced accordingly by an increase of the bolometric photon luminosity. For the top spectrum in Fig. 6 in particular, we estimated the decrease in the neutrino luminosity after inclusion of pion cooling to be  $\Delta L_\nu \simeq 0.4 \times 10^{51}$  erg/s. This would be translated to a slight increase of the bolometric luminosity, i.e.  $L_\gamma^{\text{tot}} \sim 4.4 \times 10^{51}$  erg/s instead of  $4 \times 10^{51}$  erg/s that is the value we obtain when we neglect pion synchrotron losses. Thus, the limits derived for  $\eta_{\text{p}}$  are robust, while the values of  $\zeta_{\nu,\text{max}}$  and  $\eta_{\nu,\text{max}}$  listed in Table 3 should be lower by a factor of a few.

It has been already pointed out by various authors (e.g. WB97, Asano 2005), that the photopion processes is the dominant energy loss mechanism of high-energy protons in sources with large photon compactnesses. This is also illustrated in Fig. 7, where we plot the ratio  $p_i$  of the proton energy loss rate due to a process  $i$  (synchrotron, Bethe-Heitler and photopion) to the total energy loss rate. The photopion process dominates indeed, over all other processes for the whole range of  $\eta_{\text{p}}$  values. This is also the case for the other values of  $\ell_\gamma$ .

The contribution of the Bethe-Heitler process to the hadronic cascade, however, is not always negligible. The main reason for this is that only a part of the energy lost by the protons through photopion interactions contributes to the hadronic cascade itself; the rest goes to the neutrino and high-energy neutron components. This is exemplified in Fig. 8, where we plot  $q_{\text{BH}}$  and  $q_\pi$  as a function of  $\eta_{\text{p}}$  for  $\ell_\gamma = 0.7$  and two values of the magnetic field marked on the plot. Here,  $q_{\text{BH}}$  and  $q_\pi$  are the energy injection rates defined as  $q_{\text{BH}} = \dot{E}_{\text{BH}}/\dot{E}_{\text{tot}}$  and  $q_\pi = (\dot{E}_{p\gamma}^{\pi^\pm \rightarrow e^\pm} + \dot{E}_{p\gamma}^{\pi^0 \rightarrow \gamma\gamma})/\dot{E}_{\text{tot}}$ , where  $\dot{E}_k$  denotes the energy injection rate of the process  $k$  into secondary pairs and/or photons. The dependance of the ratios  $q_{\text{BH}}$  and  $q_{p\gamma}$  on  $\eta_{\text{p}}$  is non-trivial and it is mainly determined by the characteristics of the target photon field, e.g. spectral shape and compactness, which highlights once again the role of the HC. From a quantitative point of view, we find that for intermediate values of  $\eta_{\text{p}}$  the contribution of the Bethe-Heitler process to the HC may exceed 50% and 30% for the high and low magnetic field values, respectively.

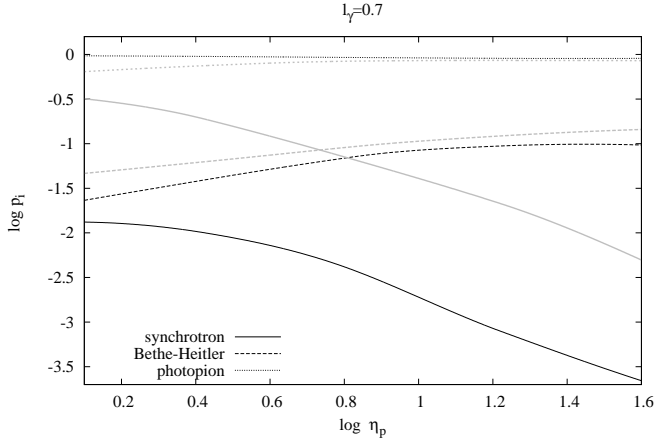


**Figure 7.** Plot of the contribution of synchrotron (solid lines), photopion (dotted lines) and Bethe-Heitler (dashed lines) energy loss rates to the total energy loss rate of protons as a function of the ratio  $\eta_p$  for  $\ell_\gamma = 0.7$  and two values of the magnetic field strength:  $B = 960$  G (black lines) and  $B = 1.5 \times 10^4$  G (grey lines). Here,  $\log \eta_p > 0.8$  corresponds to HC dominant cases. Thick lines have the same meaning as in Fig. 1.

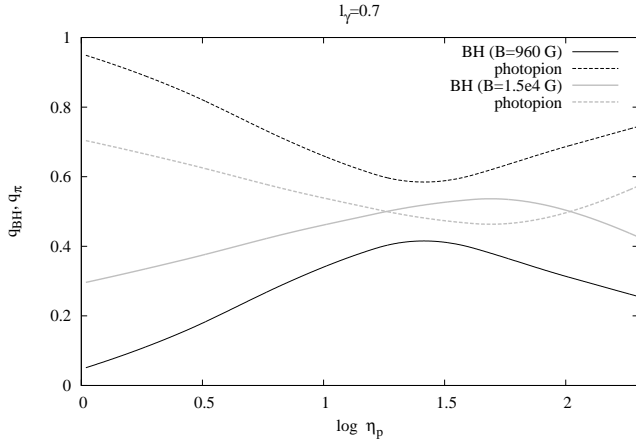


**Figure 8.** Rate of the energy injection into the hadronic cascade (pairs and photons) by the Bethe-Heitler ( $q_{BH}$ ) and the photopion ( $q_\pi$ ) processes as a function of the ratio  $\eta_p$ , for  $\ell_\gamma = 0.7$  and two values of the magnetic field strength:  $B = 960$  G (black lines) and  $B = 1.5 \times 10^4$  G (grey lines). Here,  $\log \eta_p > 0.8$  corresponds to HC dominant cases.

#### 4.4.2 Shape of GRB spectrum

As stated in §2, we adopted a fiducial photon spectrum to describe the GRB prompt emission. We chose, in particular, a grey-body photon field that can be described only by two parameters and can give us insight on the effects of the hadronic cascade mainly because of its narrow spectral energy distribution. In this section we investigate the implications of the above choice on the results presented so far, such as the maximum ratio of proton to gamma-ray luminosity.

The gamma-ray spectrum of the prompt emission can

**Table 3.** Same as in Table 2 but for  $B = 1.5 \times 10^4$  G.

$\ell_\gamma$	$\eta_{p,\max}$	$\eta_{\nu,\max}$	$\zeta_{\nu,\max}$	$\xi_{\text{sec},\max}$ (%)	$\xi_{\nu,\max}$ (%)
0.07	66	1	0.5	7	3
0.7	16.5	1	0.32	14	6
7	10.4	1.2	0.35	30	14

be successfully modelled, at least in most cases<sup>5</sup>, by the so-called ‘Band function’ (Band et al. 1993, 2009). For the purposes of the present work, it is sufficient to assume a ‘Band-like’ photon spectrum and repeat the procedure of §4.3, without getting into the details of the emission mechanism itself. We model the gamma-ray photon spectrum as  $n_\gamma \propto x^{-\alpha}$ , for  $x_{\min} < x < x_{\text{br}}$  and  $n_\gamma \propto x^{-\beta}$ , for  $x_{\text{br}} < x < x_{\max}$ , where  $\alpha = 1.2$ ,  $\beta = 2.2$ ,  $x_{\min} = 3 \times 10^{-6}$ ,  $x_{\text{br}} = 3 \times 10^{-3}$ ,  $x_{\max} = 0.3$  and  $x$  is the photon energy as measured in the comoving frame, in units of  $m_e c^2$ . The gamma-ray photon compactness can be also written as

$$\ell_\gamma = \frac{\sigma_T r_b u_\gamma}{m_e c^2}, \quad (6)$$

where

$$u_\gamma = \frac{L_\gamma}{4\pi c r_b^2 \Gamma^4} \quad (7)$$

is the energy density of the photon field in the comoving frame.

A comparison of the multiwavelength photon spectra and neutrino spectra obtained for  $\ell_\gamma = 0.7$  and two different initial gamma-ray photon fields is shown in Fig. 9. In the case of a Band-like initial photon field, we find that  $\eta_{p,\max} = 10.4$ , i.e. smaller by a factor of 1.6 than the one derived in the case of a grey-body photon spectrum. This small decrease is found also for other values of the initial photon compactness (see Table 4), and it can be understood as follows: in the case of a Band-like photon field, the same gamma-ray luminosity or compactness as before is now distributed over a wider energy range. This increases, therefore, the possible combinations of proton and photon energies with  $\gamma_p x$  that lies above the threshold for Bethe-Heitler pair production and/or pion production, and slightly enhances the emission from the secondaries. Thus, for the same magnetic field strength, the marginal curve  $\eta_{p,\max}(\ell_\gamma)$  derived for a grey-body photon spectrum (see Fig. 5) should be shifted towards smaller values by a factor of  $\sim 1.6$ .

Furthermore, the values listed in Table 4 imply the following rough scaling relations,

- $L_p \sim 25L_\gamma$ ,  $L_\nu \sim 0.5L_\gamma$  and  $L_\nu \sim 0.2L_\gamma^{\text{tot}}$ , for  $\ell_\gamma \ll 1$
- $L_p \sim L_\gamma$ ,  $L_\nu \sim 0.8L_\gamma$  and  $L_\nu \sim 0.3L_\gamma^{\text{tot}}$ , for  $\ell_\gamma \gg 1$ ,

which are robust within a factor of 2 – see previous section for the effects of the magnetic field strength. The values  $\ell_\gamma = 30$  and 70 correspond to observed gamma-ray luminosities  $4 \times 10^{52}$  erg/s and  $10^{53}$  erg/s, respectively. Thus,

<sup>5</sup> GRB spectra that cannot be adequately fitted by the Band model, either show evidence of some black-body component (e.g. Axelsson et al. 2012) or require an additional power-law component (e.g. Guiriec et al. 2010).

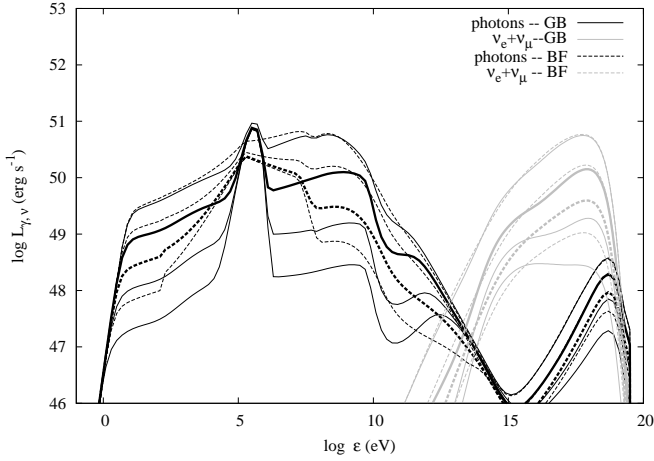


**Figure 9.** Comparison of photon and neutrino spectra for  $\ell_\gamma = 0.7$  and two different prompt gamma-ray spectra, i.e. a grey-body photon field (GB) and a Band function spectrum (BF) shown with solid and dashed lines, respectively. The proton injection compactness ranges between  $10^{-3}$  (bottom curve) and  $10^{-1.8}$  (top curve) with logarithmic increments of 0.4.

**Table 4.** Same as in Table 2 but for a ‘Band-like’ gamma-ray spectrum and two additional values of  $\ell_\gamma$ .

$\ell_\gamma$	$\eta_{p,\max}$	$\eta_{\nu,\max}$	$\zeta_{\nu,\max}$	$\xi_{\text{sec},\max}$ (%)	$\xi_{\nu,\max}$ (%)
0.07	41.6	0.5	0.2	1.3	0.7
0.7	10.4	0.5	0.2	6	3
7	6.6	0.8	0.5	17	13
15	3	0.5	0.4	21	17
30	2	0.8	0.3	26	20
70	1.6	1.0	0.3	53	60

the derived values for the various efficiencies are representative for typical and bright GRBs (e.g. Wanderman & Piran 2010). Even if  $\eta_{p,\max} \sim 1 - 2$  for the brightest GRBs, we still find  $L_\nu/L_\gamma \gtrsim 1$  and thus, these can be still considered significant neutrino emitters.

Besides the marginal effects on the ratios  $\eta_p$  and  $\zeta_\nu$ , we find that the neutrino spectra become harder (see grey lines in Fig. 9). This, however, should not be considered as a general result, since simulations with Band-like photon spectra and higher  $\ell_\gamma$  resulted in flat (in  $\nu F_\nu$  units) neutrino spectra, i.e. similar to those in Fig. 3. Our results indicate that for intermediate photon compactnesses, e.g.  $\ell_\gamma \sim 1$ , the shape of the neutrino spectra is sensitive to various parameters, such as the magnetic field strength (see Fig. 6) and the shape of the initial gamma-ray spectrum, and may deviate from the expected power-law form  $\epsilon_\nu^{-2}$ . This requires further investigation which, however, is outside the scope of the present work.

#### 4.4.3 Lorentz factor

For the benchmark case we chose a moderate value of the Lorentz factor (see §2). Since there is no reason for excluding values  $> 300$  *a priori*, here we examine the implications of a larger  $\Gamma$  on our results. The choice of a larger value of  $\Gamma$  has a twofold effect: the peak energy of the GRB spectrum

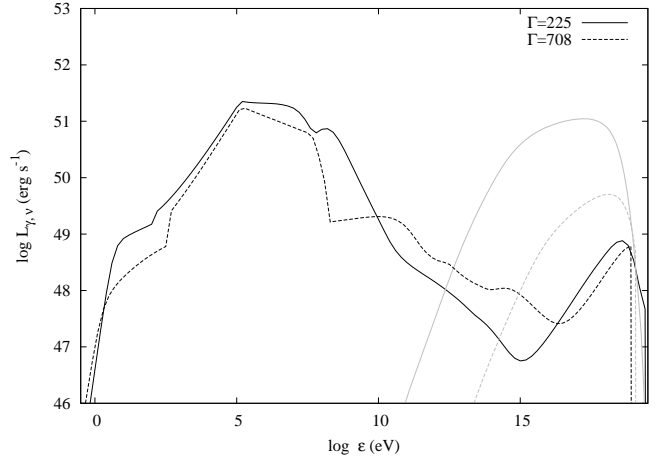


**Figure 10.** Photon (black lines) and neutrino (grey lines) spectra for  $\Gamma = 225$  and  $\Gamma = 708$  shown with solid and dashed lines, respectively. Other parameters used are:  $r_b = 10^{12}$  cm,  $B = 960$  G,  $L_\gamma = 10^{52}$  erg/s,  $L_p = 6.6L_\gamma$  and  $\gamma_{\max} = 4 \times 10^8$ .

as measured in the comoving frame decreases and the photon compactness drops significantly, since  $\ell_\gamma \propto r_b^{-1}\Gamma^{-4}$ . We showed that the maximum baryon loading given by  $\eta_{p,\max}$  increases as the emission region becomes less compact in gamma-rays (see Fig. 5), whereas the efficiency in the production of secondaries, such as pairs and neutrinos, drops (see e.g. Table 4).

As an indicative example, we choose the case with  $\ell_\gamma = 7$  and a three times larger  $\Gamma$  than before, i.e.  $\Gamma = 708$ . The photon compactness now becomes 0.07 and the peak energy of the Band spectrum decreases by a factor of three, i.e.  $x_{br} = 10^{-3}$ . Following the same steps as in §4.2, we find  $\eta_{p,\max} = 42$ . The various efficiencies are  $\eta_{\nu,\max} = 0.5$ ,  $\zeta_{\nu,\max} = 0.2$ ,  $\xi_{\text{sec},\max} = 0.02$ ,  $\xi_{\nu,\max} = 0.02$  and should be compared with the values listed in Table 4 for  $\ell_\gamma = 7$ . To illustrate better the above, we compare the photon and neutrino spectra between two cases for  $\Gamma = 225$  and  $708$ . The rest of the parameters, which are kept fixed, are:  $r_b = 10^{12}$  cm,  $B = 960$  G,  $L_\gamma = 10^{52}$  erg/s,  $L_p = 6.6L_\gamma$  and  $\gamma_{\max} = 4 \times 10^8$ . The photon and neutrino spectra are shown in Fig. 10. Note that the distortion of the gamma-ray spectrum becomes evident only for the first case (black lines), since  $\eta_p = \eta_{p,\max} = 6.6$  (see Table 4). The main reason for the differences seen in the photon spectra above  $\sim 100$  MeV and in the neutrino emission is the photon compactness, which is decisive for both the intrinsic optical depth for  $\gamma\gamma$  absorption and the efficiency of photopion production (see also Asano et al. 2009). Finally, the lower peak photon energy in the comoving frame proves to be not as important as the lower value of  $\ell_\gamma$ .

## 5 COMPARISON WITH OTHER WORKS

In this section we attempt a comparison of our results regarding the maximum value of  $\eta_p$  imposed by the hadronic cascade with other works in the literature. Our results are summarized in Fig. 11, where the solid line denotes the maximum value  $\eta_{p,\max}$  as a function of the gamma-ray compactness, which divides the  $\eta_p - \ell_\gamma$  into two regions. Above the



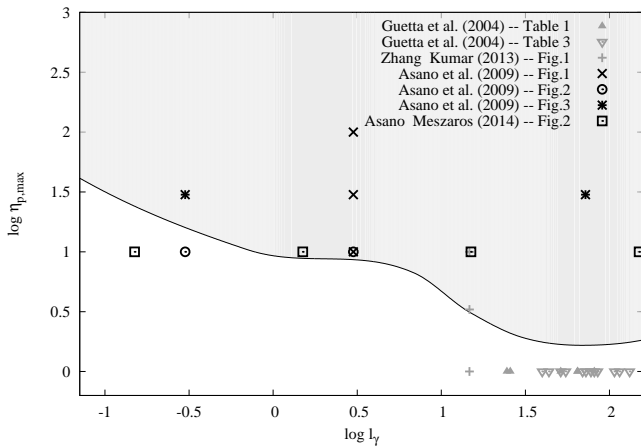


**Figure 11.** The upper limit  $\eta_{p,\max}$  plotted as a function of  $\ell_\gamma$  (solid line) along with indicative values derived from studies that focus on the diffuse GRB neutrino emission (grey symbols) and on the HC emission (black symbols). The emission from the HC distorts the GRB spectrum for parameter values drawn from the grey-colored region.

curve (grey colored region) the effects of the HC on the initial gamma-ray spectrum become prominent, whereas the combination of  $\eta_p$  and  $\ell_\gamma$  values drawn from the region below the curve does not lead to strong secondary emission.

The steps for deriving  $\eta_{p,\max}$  for different values of  $\ell_\gamma$  are the same as those described in §4.3. Here, we assume a Band function spectrum with fixed photon indices  $\alpha, \beta$  and characteristic energies  $x_{\min}, x_{\text{br}}$  and  $x_{\max}$  as described in §4.4, since this is a common assumption in most studies<sup>6</sup>. The magnetic field is taken to be  $B = 960$  G. We note also that the limiting curve in Fig. 11 may be shifted for different values of the spectral indices or/and of the break energy (see also §4.4), but no more than by a factor of 2-3. Thus, the upper limit shown in Fig. 11 can be considered robust within this factor.

The points shown in Fig. 11 correspond to different parameter sets studied in the literature. In particular, grey colored symbols correspond to studies of the neutrino flux from GRBs, whereas black colored symbols denote works that focus on the induced hadronic cascades. A comparison between our upper limit and other works is possible by, first, noting that the parameter  $\eta_p = L_p/L_\gamma$  used here is equivalent to: (i) the parameter  $f_{\gamma/p}^{-1}$  in Zhang & Kumar (2013), (ii) the ratio  $\epsilon_p/\epsilon_e$  in Asano et al. (2009), (iii) the ratio of total energies in protons and gamma-rays in Guetta et al. (2004), and (iv) the parameter  $f_p$  in Asano & Meszaros (2014). For the derivation of  $\ell_\gamma$  (see eq. (6)) we combined various parameters given in the aforementioned works, namely  $\Gamma$ ,  $r$ ,  $\delta t$ , and  $L_\gamma$  with eq. (7). We note that  $r = f_v c \Gamma^2 \delta t$ , where  $f_v$  is a numerical factor that ranges between 1-2 among the various studies. For the compilation of Fig. 11, we used the value of  $f_v$  as given in each work.

Let us focus first on the black colored symbols. Most

of the points that lie above our upper limit correspond to cases with significant modifications of the gamma-ray spectrum because of the HC in agreement with the respective studies. For example, the first two curves from top of Fig. 3 in Asano et al. (2009) are indicative cases of proton-cascade dominated spectra. Using the same values as in Asano et al. (2009), we find that the gamma-ray compactness is  $\ell_\gamma = 0.3$  and 72 for  $\Gamma = 300$  and 100, respectively. These are shown as black stars in Fig. 11. Given that the depicted values are obtained for a wide range of physical parameters, such as  $\Gamma$ ,  $L_\gamma$  and  $r_b$ , the plane  $\eta_p - \ell_\gamma$  proves to be a robust tool for distinguishing between cases with dominant hadronic cascade or not. For the former, the neutrino and secondary production efficiencies may exceed the maximum values derived in previous sections (see also Fig. 4). GeV bright GRBs detected by *Fermi*-LAT are a good example of bursts that deviate from the ‘typical’ ones (e.g. Racusin et al. 2008; Abdo et al. 2009). Assuming that their high-energy emission is a result of the hadronic initiated cascade (e.g. Asano et al. 2010), these bursts might fall into the grey-colored region of Fig. 11 depending on the relative ratio of the GeV/MeV fluxes: bright bursts with comparable fluxes in the two energy bands would be also a good candidate source of bright neutrino emission.

The grey colored symbols lie, in general, at the right part of the  $\eta_p - \ell_\gamma$  plane, since high gamma-ray compactnesses are required for efficient neutrino production. Interestingly, most of these points lie below but close (within a factor of two) to our limiting curve. For example, if a similar analysis to the one by Guetta et al. (2004) was performed, but for a higher ratio of proton to gamma-ray luminosities, e.g.  $\eta_p > 3$ , the distortion of the *pre-assumed* GRB spectrum could not be avoided. Thus, in the regime of large gamma-ray compactnesses the calculation of the neutrino emission necessitates the treatment of the secondary photon emission as well.

Note that the above discussion does not necessarily refer to bright GRBs. Because of the strong dependance of the gamma-ray compactness to the Lorentz factor, namely  $\ell_\gamma \propto L_\gamma/\Gamma^5 \delta t$ , a typical burst with  $L_\gamma = 3 \times 10^{52}$  erg/s may have ten times larger  $\ell_\gamma$  than a bright GRB with  $L_\gamma = 10^{54}$  erg/s, if its bulk Lorentz factor is by a factor of three smaller. It is noteworthy that the same conclusion is reached using different argumentation by Asano & Meszaros (2014). Although  $L_\gamma$  is relatively constrained and it lies in the range  $10^{51} - 10^{53}$  erg/s, there is freedom in the choice of  $\Gamma$  and  $\delta t$ , which makes impossible the definition of an observationally typical  $\ell_\gamma$ . Thus, studying the effects of the hadronic cascade using as a free parameter the gamma-ray compactness covers a wide range of GRBs and may facilitate future parameter studies of GRB neutrino emission.

## 6 SUMMARY AND DISCUSSION

We investigated the effects of hadronic cascades on the gamma-ray burst (GRB) prompt emission spectra in scenarios of efficient neutrino production. For this, we employed a generic method where we approximated the prompt GRB emission by either a grey-body or a Band-function spectrum, while we used as free parameters the proton injection and the prompt gamma-ray compactnesses. Using a numerical code

<sup>6</sup> The gamma-ray spectrum in Asano et al. (2009) is the result of synchrotron radiation of relativistic electrons, which, however, may be described by a Band function.

that follows the evolution of the proton, photon, neutrino and pair distributions both in energy and time, we calculated the steady-state photon and neutrino emission spectra taking into account in a self-consistent way the formation of the hadronic cascade. We showed that for each value of the gamma-ray compactness one can set an upper limit to the ratio of the proton to gamma-ray luminosity by using the fact that the emission from the hadronic cascade cannot always be neglected. On the contrary, it is an important ingredient of GRB hadronic models and it may significantly affect the overall photon and neutrino emission.

The recent PeV neutrino detection by the IceCube Collaboration (IceCube Collaboration 2013) is beginning to place stronger constraints on the parameter values used in various GRB models (Zhang & Kumar 2013). Using a detailed example (see Fig. 4) we pointed out that parameter sets that lead to high neutrino luminosities ( $\eta_\nu = L_\nu/L_\gamma \gg 1$ ) also result in modified gamma-ray photon spectra due to the emission from the hadronic cascade. On the other hand, we showed that the ratio  $\eta_{\nu,\max}$ , which is derived for parameter values just before the dominance of the hadronic cascade, lies in the range 0.5 – 1.4. Higher values are obtained for stronger magnetic fields (see Table 3) and for harder/softer GRB spectra below/above the peak, i.e. for spectra more similar to a grey-body photon emission (see Tables 2 and 4). Using this upper limit on the ratio  $L_\nu/L_\gamma$  from a single burst, we can make a rough estimate of the neutrino energy flux as follows. First, we use  $\bar{\eta}_\nu = 0.8$  as an indicative value. Then, for a burst with  $L_\gamma = 10^{52}$  erg/s we adopt  $E_\gamma = 4 \times 10^{52}$  erg as the typical energy emitted in gamma-rays (Ghirlanda et al. 2012; Kakuwa et al. 2012). For the GRB rate at the local universe we use  $R_{\text{GRB}} \simeq 1 \text{ Gpc}^{-3} \text{ yr}^{-1}$  (Wanderman & Piran 2010). We find that the energy production rate of gamma-rays per unit volume is  $\dot{U}_\gamma \simeq 4 \times 10^{43} E_{\gamma,52.6} \text{ erg Mpc}^{-3} \text{ yr}^{-1}$ . Then, the present day all-flavour neutrino energy density is given by  $U_\nu \approx \bar{\eta}_\nu \dot{U}_\gamma T$ , where  $T \simeq 10^{10} \text{ yr}$  is the Hubble time. Finally, the neutrino flux is given by

$$E_\nu^2 \Phi_\nu \approx \frac{c}{4\pi} U_\nu \approx 10^{-8} \frac{\bar{\eta}_\nu}{0.8} E_{\gamma,52.6} \text{ GeV cm}^{-2} \text{ s}^{-1} \text{ sr}^{-1}. \quad (8)$$

The above rough estimate is lower only by a factor of  $\sim 3$  than the WB upper bound (Waxman & Bahcall 1999) and the neutrino excess measured in the IceCube signal (IceCube Collaboration 2013) and, interestingly enough, this was obtained using an indirect method, i.e. using arguments about the HC dominance on the GRB photon spectra. An implicit assumption for the above derivation is that typical GRBs are the source of the PeV neutrino emission observed with IceCube. The non-detection of neutrinos from *Fermi* triggered GRBs, however, starts to challenge this assumption (e.g. Abbasi et al. 2012; He et al. 2012; Liu & Wang 2013). Even if future observations work against this scenario, models where low-luminosity GRBs ( $\sim 10^{47}$  erg/s) are the main contributors to the diffuse PeV emission cannot be ruled out, as long as the statistics of their population remains undetermined (see e.g. Cholis & Hooper 2013; Murase & Ioka 2013 for relevant discussion). Since the analysis presented here is not based on the absolute value of the GRB luminosity but on parameters that characterize the intrinsic properties of the emission region, one can re-

peat the above calculation using the appropriate values for  $E_\gamma$ ,  $R_{\text{GRB}}$  and  $\bar{\eta}_\nu$ .

Our results also indicate that a higher value for the neutrino flux is possible if  $\eta_{\nu,\max} \gtrsim 1.3$ , which further implies that if the observed neutrino signal has indeed a GRB origin then typical GRB sources should be strongly magnetized with  $B$  above a few kG (see §4.4.1) and with significant contribution of the hadronic cascade to the overall emission. Going one step further, one can argue that diffuse neutrino emission models that do not follow in detail the formation of the hadronic cascade may give fluxes erroneously close to or even above the WB upper bound simply because their parameters are pushed into the HC dominance regime. An additional feature of the high-energy neutrino spectrum in the case of a strong magnetic field would be a cutoff at a few PeV because of strong synchrotron cooling of pions and muons. It can be shown that for  $B = 10^5 \text{ G}$ ,  $r = 10^{13} \text{ cm}$  and  $\Gamma = 300$  the spectrum of muons produced via pion decay has a cutoff at  $\sim 10 \text{ PeV}$  (e.g. He et al. 2012).

The shape of the neutrino spectra is strongly affected by the photon spectrum that serves as a target field for photopion interactions and, hence, for neutrino production. Although the emitted neutrino spectra are expected to be flat in  $\nu F_\nu$  units whenever the cooling of a  $\gamma_p^{-2}$  proton distribution is efficient and the target spectra are ‘Band-like’, this is not always the case. Even in the simplest scenario where the only available target photon field is the Band-like gamma-ray emission, the neutrino spectral shape also depends on the particular pion production channel, e.g.  $\Delta^+$  resonance or multipion production channel, that is responsible for the neutrino emission at the specific energy band (Baerwald et al. 2011). To make things even more complicated, photons produced by neutral pion decay or emitted by secondary relativistic pairs through synchrotron and inverse Compton scattering contribute to the overall multi-wavelength emission and may serve as targets for photopion interactions, too. The spectral shape of the hadronic cascade emission is, therefore, an important factor for the determination of the final neutrino spectral shape.

Furthermore, our analysis showed that the investigation of the available parameter space in GRB models may be significantly simplified if this is performed using as basic variables the proton and gamma-ray compactnesses instead of the typical GRB model parameters, such as the bulk Lorentz factor and the observed isotropic gamma-ray luminosity. After all, it is the compactness of the emitting region in terms of relativistic protons and photons that mainly determines the efficiencies of the neutrino and secondary particle production.

Finally, we demonstrated through indicative examples the role of the Bethe-Heitler process in the formation of the hadronic cascade. This is not always negligible, as its contribution to the injection of secondary pairs into the hadronic cascade may exceed 30-50% for  $\ell_\gamma \sim 0.01 - 1$ , while stronger magnetic fields tend to enhance the role of the Bethe-Heitler process. However, we find that its contribution is significantly suppressed for  $\ell_\gamma \gg 10$ .

We have explored the role of hadronic cascades in GRB models of efficient neutrino production using a method that is sufficiently generic to be applicable to different scenarios of prompt GRB emission. Assuming that GRBs are the sources of the TeV-PeV neutrinos detected by IceCube, then

our results suggest that GRBs can account for the current neutrino flux level only if there is a substantial contribution of the hadronic emission to the overall GRB photon spectra.

## ACKNOWLEDGEMENTS

I would like to thank Dr. S. Dimitrakoudis for providing the numerical code and Professors A. Mastichiadis and D. Giannios for fruitful discussions and comments on the manuscript. I would also like to thank the anonymous referee for his/her comments that helped to improve the manuscript. Support for this work was provided by NASA through Einstein Postdoctoral Fellowship grant number PF 140113 awarded by the Chandra X-ray Center, which is operated by the Smithsonian Astrophysical Observatory for NASA under contract NAS8-03060.

## REFERENCES

- Aartsen M. G. et al., 2014, ArXiv e-prints  
 Abbasi R. et al., 2012, *Nature*, 484, 351  
 Abbasi R. et al., 2010, *ApJ*, 710, 346  
 Abdo A. A. et al., 2009, *ApJL*, 706, L138  
 Aharonian F. A., 2000, *New Astronomy*, 5, 377  
 Asano K., 2005, *ApJ*, 623, 967  
 Asano K., Guiriec S., Mészáros P., 2009, *ApJL*, 705, L191  
 Asano K., Inoue S., 2007, *ApJ*, 671, 645  
 Asano K., Inoue S., Mészáros P., 2010, *ApJL*, 725, L121  
 Asano K., Meszaros P., 2014, ArXiv e-prints  
 Axelsson M. et al., 2012, *ApJL*, 757, L31  
 Baerwald P., Bustamante M., Winter W., 2013, *ApJ*, 768, 186  
 Baerwald P., Hümmer S., Winter W., 2011, *PhysRevD*, 83, 067303  
 Band D. et al., 1993, *ApJ*, 413, 281  
 Band D. L. et al., 2009, *ApJ*, 701, 1673  
 Böttcher M., Dermer C. D., 1998, *ApJL*, 499, L131  
 Cholis I., Hooper D., 2013, *JCAP*, 6, 30  
 Coppi P. S., Blandford R. D., 1990, *MNRAS*, 245, 453  
 Dermer C. D., 2010, in *American Institute of Physics Conference Series*, Vol. 1279, American Institute of Physics Conference Series, Kawai N., Nagataki S., eds., pp. 191–199  
 Dermer C. D., Atoyan A., 2003, *Physical Review Letters*, 91, 071102  
 Dimitrakoudis S., Mastichiadis A., Protheroe R. J., Reimer A., 2012, *A&A*, 546, A120  
 Dimitrakoudis S., Petropoulou M., Mastichiadis A., 2014, *Astroparticle Physics*, 54, 61  
 Ghirlanda G., Nava L., Ghisellini G., Celotti A., Burlon D., Covino S., Melandri A., 2012, *MNRAS*, 420, 483  
 Guetta D., Hooper D., Alvarez-Mun˜ız J., Halzen F., Reuveni E., 2004, *Astroparticle Physics*, 20, 429  
 Guiriec S. et al., 2010, *ApJ*, 725, 225  
 He H.-N., Liu R.-Y., Wang X.-Y., Nagataki S., Murase K., Dai Z.-G., 2012, *ApJ*, 752, 29  
 Hillas A. M., 1984, *ARA&A*, 22, 425  
 IceCube Collaboration, 2013, *Science*, 342  
 Kakuwa J., Murase K., Toma K., Inoue S., Yamazaki R., Ioka K., 2012, *MNRAS*, 425, 514

- Lightman A. P., Zdziarski A. A., 1987, *ApJ*, 319, 643  
 Liu R.-Y., Wang X.-Y., 2013, *ApJ*, 766, 73  
 Mannheim K., Protheroe R. J., Rachen J. P., 2001, *PhysRevD*, 63, 023003  
 Mastichiadis A., Kirk J. G., 1995, *A&A*, 295, 613  
 Mastichiadis A., Protheroe R. J., Kirk J. G., 2005, *A&A*, 433, 765  
 Mücke A., Engel R., Rachen J. P., Protheroe R. J., Stanev T., 2000, *Computer Physics Communications*, 124, 290  
 Murase K., 2008, *PhysRevD*, 78, 101302  
 Murase K., Ioka K., 2013, *Physical Review Letters*, 111, 121102  
 Paczynski B., Xu G., 1994, *ApJ*, 427, 708  
 Petropoulou M., Mastichiadis A., 2012, *MNRAS*, 421, 2325  
 Piran T., 2004, *Reviews of Modern Physics*, 76, 1143  
 Protheroe R. J., Johnson P. A., 1996, *Astroparticle Physics*, 4, 253  
 Rachen J. P., Mészáros P., 1998, *PhysRevD*, 58, 123005  
 Racusin J. L. et al., 2008, *Nature*, 455, 183  
 Reynoso M. M., 2014, ArXiv e-prints  
 Vietri M., 1995, *ApJ*, 453, 883  
 Wanderman D., Piran T., 2010, *MNRAS*, 406, 1944  
 Waxman E., 1995, *ApJL*, 452, L1  
 Waxman E., Bahcall J., 1997, *Physical Review Letters*, 78, 2292  
 Waxman E., Bahcall J., 1999, *PhysRevD*, 59, 023002  
 Zhang B., Kumar P., 2013, *Physical Review Letters*, 110, 121101  
 Zhang B., Mészáros P., 2004, *International Journal of Modern Physics A*, 19, 2385

## APPENDIX A: PROTON ENERGY LOSS RATE DUE TO PHOTOPION INTERACTIONS WITH A GREY-BODY PHOTON FIELD

The differential number density of a grey-body photon field is given by

$$n_\gamma(x) = n_0 \frac{x^2}{e^{x/\Theta} - 1}, \quad (9)$$

where  $x$  and  $\Theta$  are the photon energy and the effective temperature in units of  $m_e c^2$ , while the normalization  $n_0$  is related to the photon compactness  $\ell_\gamma$  as

$$n_0 = \frac{15\ell_\gamma}{\pi^4 \Theta^4 \sigma_T r_b}, \quad (10)$$

where  $r_b$  is the size of the emission region and  $\ell_\gamma$  does not violate the black-body limit. The fractional energy loss rate of a proton with energy  $E_p = \gamma_p m_p c^2$  due to photopion interactions with the above photon field is then given by (see e.g. WB97):

$$t_{p\gamma}^{-1} \equiv -\frac{1}{E_p} \frac{dE_p}{dt} \Big|_{p\gamma} = \quad (11)$$

$$= \frac{c}{2\gamma_p^2} \int_{\epsilon_{th}}^{\infty} d\epsilon \epsilon \sigma_{p\gamma}(\epsilon) \xi_{p\gamma}(\epsilon) \int_{\epsilon/2\gamma_p}^{\infty} dx x^{-2} n_\gamma(x), \quad (12)$$

where  $\epsilon$  is the photon energy (in  $m_e c^2$  units) as seen in the rest frame of the proton,  $\epsilon_{th}$  is the threshold energy of the interaction in  $m_e c^2$  units, i.e.  $\epsilon_{th} \simeq 300$ ,  $\sigma_{p\gamma}$  and

$\xi_{p\gamma}$  are the cross section and the inelasticity of the interaction, respectively. Here, we approximate the cross section by a step function, i.e.  $\sigma_{p\gamma} \approx \sigma_0 H(\epsilon - \epsilon_{\text{th}})$  with  $\sigma_0 = 5 \times 10^{-28} \text{ cm}^2 \simeq (5/6 \times 10^{-3})\sigma_T$ . Although the inelasticity may vary between  $\sim 0.1$  and  $0.5$  for interactions taking place close to and far from the threshold, respectively, for our purposes it is sufficient to use an average value, e.g.  $\bar{\xi}_{p\gamma} \approx 0.2$ .

Using these approximations and after performing the integration over  $x$ , eq. (12) simplifies into

$$t_{p\gamma}^{-1} = -\frac{c\Theta n_0 \sigma_0 \bar{\xi}_{p\gamma}}{2\gamma_p^2} \int_{\epsilon_{\text{th}}}^{\infty} d\epsilon \epsilon \ln(1 - e^{-\epsilon/2\gamma_p\Theta}). \quad (13)$$

The function that appears in the above integral, i.e.  $f(\epsilon) = -\epsilon \ln(1 - e^{-\epsilon/2\gamma_p\Theta})$ , is a steep function of  $\epsilon$  that shows a sharp peak at approximately  $\epsilon_p \simeq 1.4\gamma_p\Theta$ . Hence, its integral  $I$  can be approximated by  $I_{\text{appr}} \approx \epsilon_p f(\epsilon_p)$ , where  $f(\epsilon_p) \approx 0.7\epsilon_p$ . This is illustrated in Fig. 12, where the hatched area that corresponds to the value of  $I$  is approximated by the area below the  $\delta$ -function centered at  $\epsilon_p$ . We note here that the sharpness of the peak at  $\epsilon \simeq \epsilon_p$  is not evident because of the logarithmic scale. If we compare  $I_{\text{appr}}$  with the value  $I$  obtained after numerical integration of the integral, we find that their ratio  $f_{\text{cor}} = I/I_{\text{appr}}$  can be modeled as

$$f_{\text{cor}} \simeq 3.5 \tanh\left(\frac{\epsilon_p}{\epsilon_{\text{th}}}\right), \quad (14)$$

for  $\epsilon_p \geq \epsilon_{\text{th}}$ . In what follows, we will incorporate this ‘correction’ factor into our analytical expression. Thus, the fractional energy loss rate for protons with Lorentz factor  $\gamma_p > \epsilon_{\text{th}}/1.4\Theta$  is given by

$$t_{p\gamma}^{-1} \approx 5 \times 10^{-3} f_{\text{cor}} \frac{\ell_\gamma}{4\pi^4 t_d \Theta}, \quad (15)$$

where we have used eq. (10) and  $t_d = r_b/c$ . When normalized with respect to  $t_d$ , we find

$$\tau_{p\gamma}^{-1} \approx 1.8 \times 10^{-5} f_{\text{cor}} \frac{\ell_\gamma}{\Theta}, \quad (16)$$

which, besides the correction factor, depends only on  $\ell_\gamma$  and  $\Theta$ .

## APPENDIX B: MAXIMUM PROTON ENERGY

The maximum energy of protons is typically calculated by balancing the acceleration and energy loss rates. An independent constraint comes from the so-called Hillas criterion (Hillas 1984) according to which, the gyroradius of the most energetic particles should not exceed the size of the emission region. Here we compare the different upper limits on the maximum proton energy.

In the simplest scenario protons are accelerated at a rate which is inverse proportional to their energy, namely  $t_{\text{acc}}^{-1}(\gamma) = \kappa e B c / \gamma m_p c^2$ , where  $\kappa$  is an efficiency factor. For simplicity, we assume  $\kappa = 1$ . As long as proton acceleration takes place at small Thomson optical depths, the main energy loss processes that act competitive to the acceleration process are synchrotron radiation and photopion interactions. Note that for larger optical depths pp-collisions

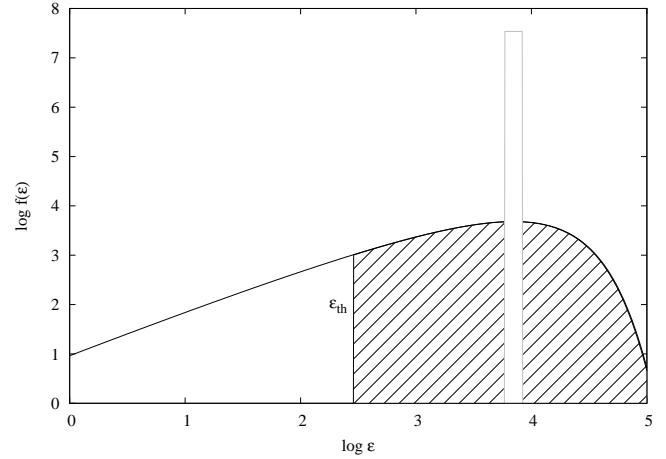


**Figure 12.** Function  $f = -\epsilon \ln(1 - e^{-\epsilon/\epsilon_0})$  for  $\epsilon_0 = 10^4$  (black line) and the  $\delta$ -function approximation (grey line). The hatched area denotes  $I$  while the white colored area below the delta function corresponds to  $I_{\text{appr}}$ .

consist another important energy loss mechanism for protons as well as another neutrino production channel (e.g. Murase 2008).

The synchrotron proton loss timescale is given by  $t_{\text{syn}} = 6\pi m_p c \chi^2 / \sigma_T B^2 \gamma$ , where  $\chi = m_p/m_e$ . By equating  $t_{\text{acc}}$  and  $t_{\text{syn}}$  and by using eq. (1) and  $r_b \approx c\Gamma\delta t$  we find the saturation Lorentz factor because of synchrotron losses

$$\gamma_{\text{syn}} \simeq 9 \times 10^8 \Gamma_2^{3/2} \delta t_{-1}^{1/2} L_{j,52}^{-1/4} \epsilon_{B,-1}^{-1/4}. \quad (17)$$

For the benchmark case of  $\Gamma = 225$ ,  $\delta t \approx 0.15 \text{ s}$ ,  $\epsilon_B = 2.2 \times 10^{-3}$  and  $L_j = 3 \times 10^{52} \text{ erg/s}$ , we find  $\gamma_{\text{syn}} \simeq 7 \times 10^9 > \gamma_H$ . Even for  $B = 1.5 \times 10^4 \text{ G}$  (see §4.4.1) the relation  $\gamma_{\text{syn}} > \gamma_H$  holds.

For large values of the photon compactness, proton cooling due to photopion production may overcome synchrotron losses. The respective loss rate for protons having energies above the threshold is constant and is given by eq. (5); for the derivation, see Appendix A. Setting  $t_{\text{acc}} = t_{p\gamma}$  we find the saturation Lorentz factor to be

$$\gamma_{p\gamma} \simeq 2 \times 10^9 \Gamma_2^2 \delta t_{-1}^{1/2} \epsilon_{B,-1}^{1/2} L_{j,52}^{1/2} L_{\gamma,52}^{-1} \frac{E_{\text{br,obs}}}{0.5 \text{ MeV}} (1+z), \quad (18)$$

where we replaced the effective temperature  $\Theta$  in eq. (5) by the peak energy of the photon spectrum  $E_{\text{br,obs}}$ . For the benchmark parameter values we find  $\gamma_{p\gamma} \approx 3 \times 10^9 (1+z)/L_{\gamma,52} > \gamma_H$ .

Summarizing, for the present analysis it is safe to assume that  $\gamma_{\text{max}} = \gamma_H$ .